ACS OMEGA

http://pubs.acs.org/journal/acsodf
Article

Thermal Conversion of Ultrathin Nickel Hydroxide for Wide Band Gap 2D Nickel Oxides

Lu Ping,⊥ Nicholas Russo,⊥ Zifan Wang, Ching-Hsiang Yao, Kevin E. Smith,* and Xi Ling*

Cite This: *ACS Omega* 2024, 9, 44164−44172
Read Online

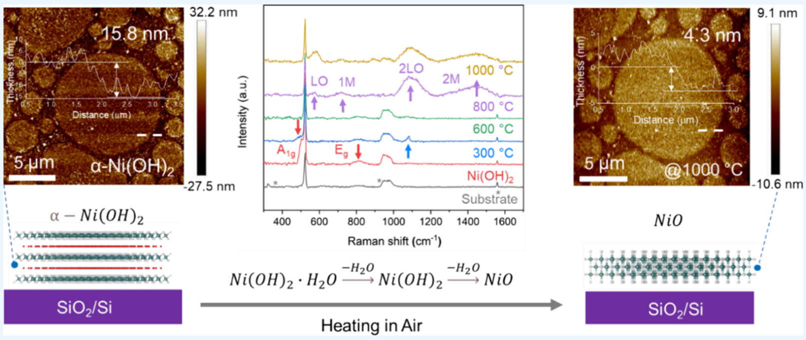

ABSTRACT: Wide band gap (WBG) semiconductors (E_g > 2.0 eV) are integral to the advancement of next-generation electronics, optoelectronics, and power industries owing to their capability for high-temperature operation, high breakdown voltage, and efficient light emission. Enhanced power efficiency and functional performance can be attained through miniaturization, specifically via the integration of device fabrication into a two-dimensional (2D) structure enabled by WBG 2D semiconductors. However, as an essential subgroup of WBG semiconductors, 2D transition metal oxides (TMOs) remain largely underexplored in terms of physical properties and applications in 2D optoelectronic devices, primarily due to the scarcity of sufficiently large 2D crystals. Thus, our goal is to develop synthesis pathways for 2D TMOs possessing large crystal domains (e.g., >10 μm), expanding the 2D TMO family and providing insights for future engineering of 2D TMOs. Here, we demonstrate the synthesis of WBG 2D nickel oxide (NiO) (E_g > 2.7 eV) thermally converted from 2D nickel hydroxide (Ni(OH)$_2$) with a lateral domain size larger than 10 μm. Moreover, the conversion process is investigated using various microscopic techniques, such as atomic force microscopy, Raman spectroscopy, transmission electron microscopy, and X-ray photoelectron spectroscopy, providing significant insights into morphology and structural variations under different oxidative conditions. The electronic structure of the converted Ni$_x$O$_y$ is further investigated using multiple soft X-ray spectroscopies, such as X-ray absorption and emission spectroscopies.

■ INTRODUCTION

Wide band gap (WBG) semiconductors, with a band gap in the range of 2.0−4.0 eV, have demonstrated great potential in the field of electronics, optoelectronics, and power industries due to their power handling capability and high-temperature resilience.[1] Specifically, direct mapping of the electric field in the device channel of gallium nitride-based high-electron-mobility transistors is achieved with submicrometer resolution, allowing for a better understanding of how electronic devices work and their potential limitations.[2] Besides, the development of ultraviolet photodetectors has flourished through the exploration of various WBG semiconductors and hybrid structures, e.g., metal (di)-chalcogenides[3] and perovskites,[4] owing to their direct light emission in the ultraviolet range. Moreover, WBG semiconductors are also widely considered the current state-of-the-art and future answer in power electronics like smart grid applications.[5] To further improve the efficiency and lower the cost, miniaturized electronic and optoelectronic devices constructed and accomplished by 2D semiconductors are believed to be the future for next-generation micro-/nanoelectronics.[6−11] So far, over a thousand possible inorganic compounds have been discovered as layered materials,[12] with a high concentration on 2D narrow band gap (NBG) semiconductors (E_g < 2.0 eV).[13−18] In contrast, the research and development on WBG 2D semiconductors (E_g > 2.0 eV) consisting of metal chalcogenides, halide system, and metal oxides (MOs) still lags behind that of conventional NBG semiconductors.[12,19,20] However, it is imperative that equal importance and emphasis are placed on advancing the

Received: April 4, 2024
Revised: August 30, 2024
Accepted: September 11, 2024
Published: October 22, 2024

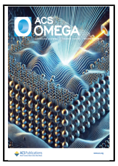

ACS Publications

https://doi.org/10.1021/acsomega.4c03253

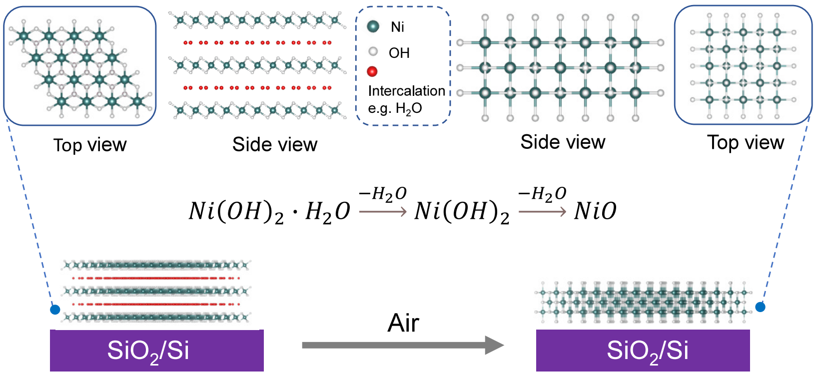

Figure 1. Schematic of thermal conversion from 2D α-$Ni(OH)_2$ to 2D NiO.

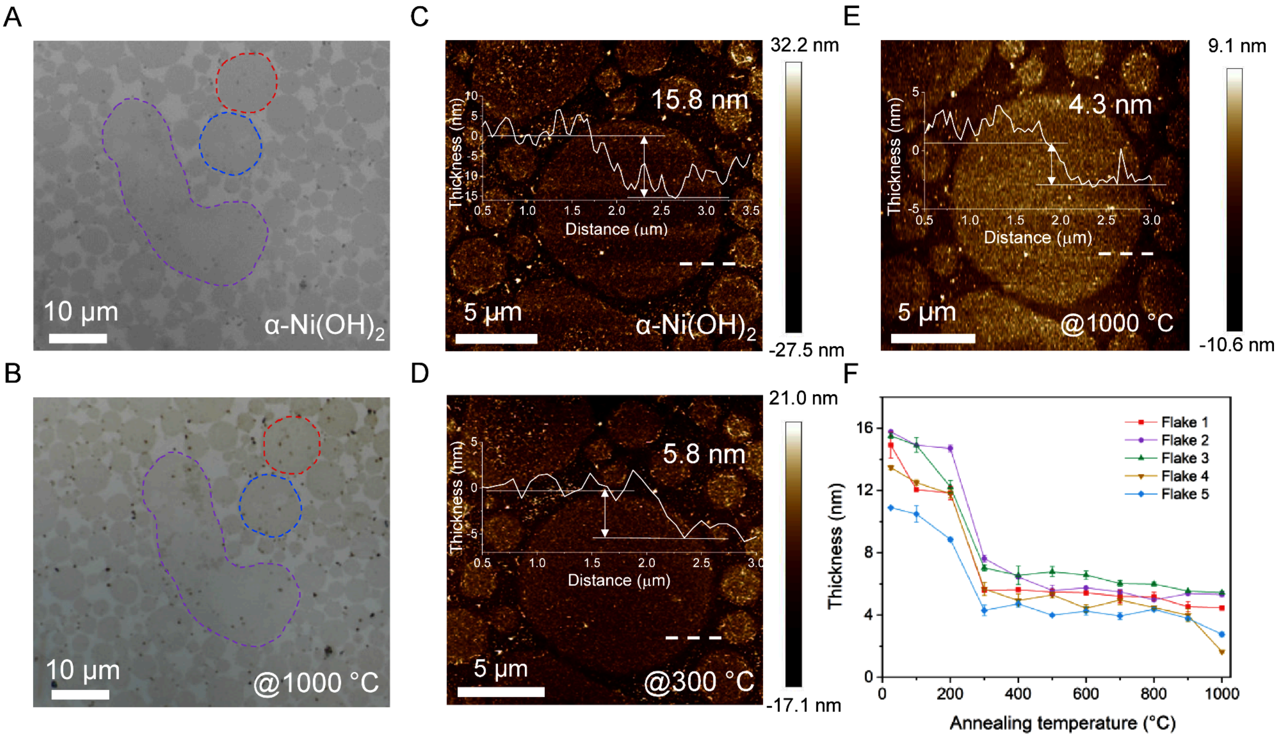

Figure 2. Morphology characterization of 2D NiO converted from 2D α-$Ni(OH)_2$. Optical images of the 2D α-$Ni(OH)_2$ sample before (A) and after 10 h oxidizing at 1000 °C (B). AFM images of the flake before (C) and after 10 h oxidizing at 300 °C (D) and 1000 °C (E). Insets: height profiles obtained along white dashed lines. Thickness variation with increased oxidizing temperature on seven 2D α-$Ni(OH)_2$ flakes (F). (C) is reprinted in part with permission from Ping, L.; Minarik, G. E.; Gao, H.; et al. Synthesis of 2D layered transition metal (Ni, Co) hydroxides via edge-on condensation. *Sci. Rep.* 2024, **14**, 3817. Copyright @2024 Springer Nature.

understanding and applications of WBG 2D semiconductors to drive the forthcoming revolution in 2D micro-/nanodevices.

Transition metal oxides (TMOs), of which the band gaps are mostly located in the range of 3.0−5.0 eV, is complementary to NBG semiconductors.[21] As an essential subset of WBG semiconductors, their bulk forms are widely applied in electronic and optoelectronic fields, benefiting from their visible-light transparency, low cost, and high stability in environments. However, the 2D form of TMOs is far less explored, although they may inherit the attracting properties of their bulk form or exhibit unprecedented properties due to quantum confinement effects and interfacial interactions.[21] Recent research has realized the preparation of several atomically thin 2D TMOs through different approaches, such as physically/chemically assisted exfoliation,[22,23] liquid metal oxidation,[24,25] and vapor phase deposition (e.g., physical or chemical vapor deposition and atomic layer deposition).[26,27] The obtained 2D TMOs have substantially expanded the scope of the 2D family for next-generation optoelectronics. For example, the recently developed novel *p*-type 2D hexagonal TiO_2 (h-TiO_2) demonstrates a high hole mobility of up to 950 $cm^2 V^{-1} s^{-1}$ in back-gated field-effect transistors (FETs);[22] photodetectors based on 2D Fe_2O_3 realize ultrabroadband response ranging from UV (375 nm) to long-wavelength infrared (10.6 μm).[28] Nevertheless, many other 2D TMOs, such as Ni_xO_y, which have demonstrated high hole mobility and fast switching speed in nano FETs,[29] are not widely realized yet. Especially, the ones with sufficiently large lateral domains (>10 μm) are essential for semiconductor device design and application. Therefore, it is highly desirable to develop synthesis strategies to fulfill this objective, paving the

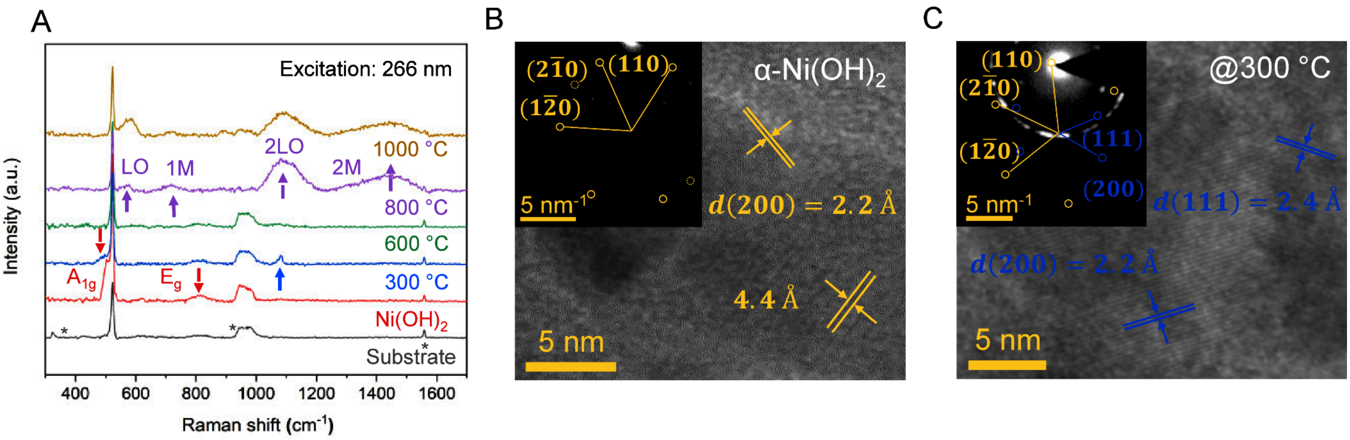

Figure 3. Identification of NiO and structural characterization. (A) Deep UV Raman spectra of 2D α-Ni(OH)$_2$, NiO-300, 600, 800, and 1000 °C and the substrate excited with a 266 nm laser. Peaks labeled with "*" are from the Si substrate. (B) High-resolution TEM image of 2D α-Ni(OH)$_2$. Inset: SAED pattern. (C) High-resolution TEM image of NiO-300. Inset: SAED pattern.

way for both fundamental study and application exploration of WBG 2D semiconductors.

In this work, we realized the synthesis of WBG 2D (>2.7 eV) NiO through a simple thermal conversion from 2D Ni(OH)$_2$. The morphology of the 2D NiO crystals closely resembles that of the precursor 2D Ni(OH)$_2$, with lateral dimensions exceeding 10 μm, as previously reported in our research.[30] Specifically, the synthesis of 2D NiO involved the air oxidation of 2D α-Ni(OH)$_2$ crystals under varying oxidizing temperatures, allowing for the establishment of structural and chemical composition changes throughout the thermal conversion process at different temperature regimes. The electronic band gaps of the resulting Ni$_x$O$_y$ (E_g > 2.7 eV) are determined using soft X-ray techniques, i.e., X-ray absorption spectroscopy (XAS) and X-ray emission spectroscopy (XES). Comparative analysis of the obtained band gap values with those of other reported WBG 2D semiconductors verified that it sits firmly in the middle range of MOs and at the higher end of metal chalcogenides and halide systems. We anticipate the insights gained from this study and the characteristics of the synthesized 2D Ni$_x$O$_y$ to offer valuable guidance for engineering 2D MOs and designing applications involving WBG 2D semiconductors.

■ RESULTS AND DISCUSSION

2D α-Ni(OH)$_2$ flakes are deposited via drop-casting on 1 × 1 cm SiO$_2$/Si substrates, and the samples undergo oxidation in air, as illustrated in the schematic presented in Figure 1. Following a 10 h oxidation process at 100 °C, the resulting sample is labeled as NiO-100 and is subjected to characterizations using various techniques. Subsequently, the sample is subjected to heating at 200 °C and maintained for 10 h, leading to NiO-200, which is characterized before undergoing further oxidation at 300 °C for an additional 10 h. The highest temperature explored and conducted in this work is 1000 °C, resulting in NiO-1000. Throughout each oxidation step, ramping and cooling rates are set at 100 °C/h, ensuring a steady and smooth conversion process. Multiple characterizations, such as Raman spectroscopy and XPS, are performed at each step, showing that 2D NiO starts to form at 300 °C.

Morphology Characterization of 2D NiO. Figure 2A is the optical image of an area that is covered by 2D α-Ni(OH)$_2$ flakes with three flakes contoured by red, blue, and purple dashed lines. Figure 2B is the optical image of the same area after converting it to 2D NiO-300, showing that the three contoured flakes stay in their original shapes without visible decomposition. AFM is applied to track the thickness variation along the increased oxidizing temperature. As shown in Figure 2C, the thickness of this 2D α-Ni(OH)$_2$ flake is measured as 15.8 nm; at the same position, the thickness of NiO-300 decreases dramatically by 63.3% to 5.8 nm (Figure 2D), which is attributed to the removal of interlayer intercalation and the crystal structure change from hydroxide, a vdW (layered) to non-vdW oxide (close-packed). The thickness does not change significantly when the temperature further increases; it slightly decreases to 4.3 nm on NiO-1000 (Figure 2E). In general, the dramatic vertical reduction along the conversion occurs at 300 °C, as evidenced by the tracked thickness variation (Figures S1−S5) observed on five 2D α-Ni(OH)$_2$ flakes (Figure 2F). Meanwhile, a similar phenomenon is also observed in thermogravimetric analysis (TGA), which is applied to track the weight change with the increasing temperature from the starting 2D α-Ni(OH)$_2$ to 500 °C. Dramatic weight losses are observed (Figure S6) at 100 and 300 °C due to the removal of surface water and intercalation.

Structural Characterization of 2D NiO. First, Raman spectroscopy is applied to identify NiO converted from Ni(OH)$_2$ since it provides unique vibrational information and fingerprints of different materials. A deep UV laser with 266 nm wavelength (∼4.66 eV) is used to excite the resonance. As shown in Figure 3A, the characteristic peaks (red arrows) from 2D α-Ni(OH)$_2$ at 502.8 and 809.9 cm^{-1} are diminishing when the temperature is increased to 300 °C, which completely disappear when the temperature reaches 800 °C. This suggests that the 2D α-Ni(OH)$_2$ is completely consumed and converted to a new substance. Meanwhile, at 300 °C, a new peak at 1087.2 cm^{-1} rises and expands to a slightly wider peak at 600 °C, which eventually becomes distinct and significant at 800 °C and corresponds to the 2LO (longitudinal optical) mode of NiO.[31] Besides, LO, 1 M (magnon), and 2 M modes of NiO are also observed at 567.9, 718.9, and 1437.1 cm^{-1} at 800 °C,[31,32] respectively, suggesting that the conversion is complete at this temperature. All of the characteristic peaks of NiO reside at the same position when the temperature is lifted to 1000 °C. Therefore, the results

https://doi.org/10.1021/acsomega.4c03253
ACS Omega 2024, 9, 44164−44172

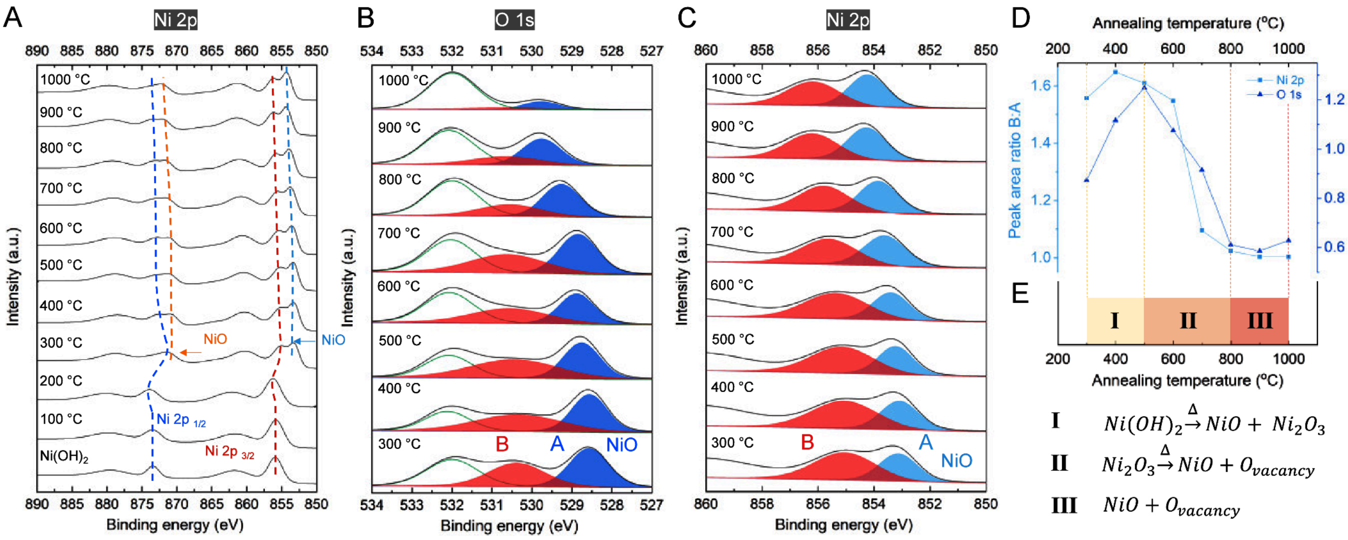

Figure 4. Investigation of the conversion process by XPS. (A) Ni 2p spectra of NiO oxidized at different temperatures from 100 to 1000 °C. (B) O 1s spectrum of NiO oxidized under different temperatures from 300 to 1000 °C (the whole range from RT to 1000 °C is shown in Figure S8). The colored area A in dark blue consists of contribution from NiO, and the colored area B in red consists of contribution from both $Ni(OH)_2$ and Ni_2O_3. (C) Ni $2p_{3/2}$ spectra from 300 to 1000 °C. The colored area A in light blue consists of contribution from NiO, and the colored area B in red consists of contribution from both $Ni(OH)_2$ and Ni_2O_3. (D) Comparison of B/A from O 1s and from Ni $2p_{3/2}$, which shows a similar trend. (E) Concluded chemical reactions during thermal conversion in three phases I, II, and III.

show that the conversion of 2D α-$Ni(OH)_2$ to 2D NiO starts at 300 °C and completes at 800 °C.

Moreover, the emergence of NiO is observed by TEM as well. A high-magnification TEM image in Figure 3B shows that the *d*-spacings between the (200) and (400) planes are 2.2 and 4.4 Å, respectively.[33] The selected area electron diffraction (SAED) (Figure 3B, inset) provides a sharp diffraction pattern and reveals the hexagonal lattice structure of $Ni(OH)_2$. Diffraction from the (110), $(2\bar{1}0)$, and $(1\bar{2}0)$ lattice planes can be observed. While on NiO-300 (Figure 3C, inset), a new diffraction pattern is observed within the original pattern, and the *d*-spacings are measured as 2.4 and 2.1 Å, corresponding to the (111) and (200) planes from NiO.[34] The spacing of these two planes can also be measured from high-magnification TEM images shown in Figure 3C, which is 2.4 and 2.2 Å for (111) and (200), respectively.[34] The 2D nature of a micrometer large domain of a typical α-$Ni(OH)_2$ flake is once again observed in the low-magnification TEM image in Figure S7.

Chemical State Variation during the Conversion. After identifying the starting and ending points of the conversion from hydroxide to oxide, we continued to investigate the entire process using XPS by characterizing the chemical states of Ni and O that occurred at different oxidizing temperatures during the conversion. First, Ni 2p spectra are collected along with the increasing oxidizing temperature and are shown in Figure 4A (separate spectrum for each sample can be found in Figure S8). In general, the most noticeable characteristic is at 300 °C, where a new peak rises up that is denoted as NiO. Specifically, Figure S8A shows the Ni 2p spectrum of the original 2D α-$Ni(OH)_2$, and a spin–orbital coupling causes splitting energy between Ni $2p_{3/2}$ (855.9 eV) and Ni $2p_{1/2}$ (873.4 eV) measured as 17.5 eV, which is characteristic of the Ni^{2+} ion in $Ni(OH)_2$.[35,36] For NiO-300 (Figure 4A), both the Ni $2p_{3/2}$ (blue arrow) and Ni $2p_{1/2}$ (orange arrow) peaks are composed of two peaks, of which the binding energy positions suggest the formation of NiO. Besides, there is no distinct change when the temperature is further lifted to 800 °C (Figure S8I) and 1000 °C (Figure S8K), suggesting that there is no new substance formed in the higher temperature range.

Meanwhile, the O 1s spectra are collected along with the increasing oxidizing temperature and are shown in Figure S9. Separate fitted spectra at each temperature are shown in Figure S10. A new peak at 528.6 eV also rises at 300 °C, which is highly consistent with our observation from the Ni 2p analysis and previous structural characterizations. Specifically, Figure S10A shows the O 1s spectrum of the original 2D α-$Ni(OH)_2$, which consists of three peaks at 531.1, 532.4, and 533.2 eV, representing Ni–O–H, O–Si–O (from the substrate), and H–O–H, respectively.[37,38] The appearance of the H–O–H signal suggests the presence of H_2O in the crystals, mainly as intercalation species between layers to form α-$Ni(OH)_2$. After the sample is oxidized at 300 °C (Figure S10D), the peak representing water completely disappears, suggesting the removal of the intercalated water, which is consistent with the dramatic thickness decrease from AFM measurements (Figure 2F). Besides, a new peak at 528.6 eV appears that is denoted as NiO, and the peak at 530.4 eV suggests the formation of Ni_2O_3.[39,40] With the increasing oxidizing temperature, the peak representing Ni_2O_3 diminishes at 800 °C (Figure S10I) and eventually almost disappears at 1000 °C (Figure S10K) due to the thermal decomposition from Ni_2O_3 to NiO.[41,42]

To prove our hypothesis of the formation and decomposition of Ni_2O_3, the peak areas in XPS across various temperatures are analyzed and compared to investigate the thermal conversion process. As shown in Figure 4B, the peak area in dark blue (area A) is solely contributed to the contribution of O^{2-} from NiO. However, the peak area in red (area B) is more complex, and it could be the contribution of O^{2-} from $Ni(OH)_2$ or from Ni_2O_3. Similarly, the peak area on Ni $2p_{3/2}$ spectra is colored as well and is shown in Figure 4C. The Peak area in light blue (area A) is contributed to Ni^{2+}

https://doi.org/10.1021/acsomega.4c03253
ACS Omega 2024, 9, 44164−44172

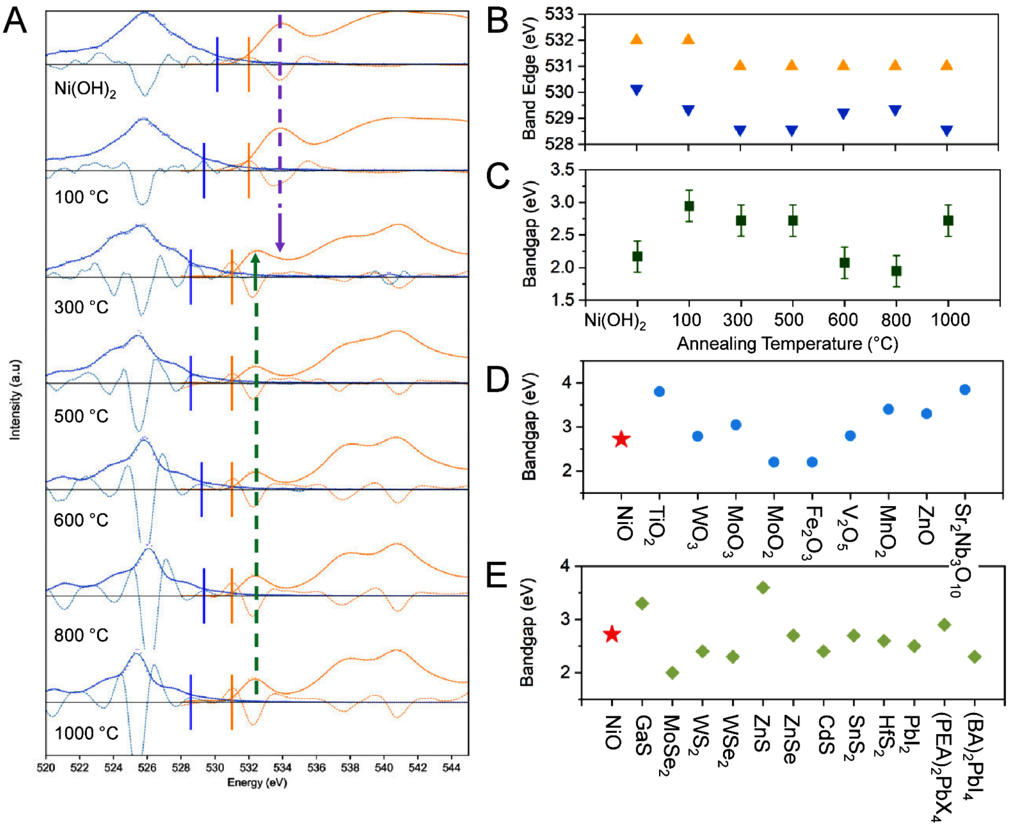

Figure 5. Electronic structure characterization of 2D $Ni(OH)_2$and NiO films using soft X-ray techniques. (A) XAS (total electron yield) (orange) and XES (blue) spectra are shown as solid lines. A Savitzky−Golay filter is applied to reduce noise and compute second derivatives (dashed lines, magnified); band onsets (short orange lines for absorption and short blue lines for emission) are determined by the first peak in the rising spectral edge above the noise level. Purple and green arrows indicate the structural change at 533.5 eV for α-$Ni(OH)_2$ and at 532.5 eV for NiO, respectively. Spectra are normalized to the highest intensity peak in each spectrum. (B) Band edges derived from absorption (orange dots) and emission (blue dots) spectra. (C) Determined band gaps, by taking the difference between absorption and emission onsets from (C) for each sample. (D) Band gap of 2D NiO (in red), in comparison to other WBG 2D oxides.[62,63] Adapted in part with permission from Chaves, A.; Azadani, J. G.; Alsalman, H.; et al. Bandgap engineering of two-dimensional semiconductor materials. *npj 2D Mater. Appl.* 2020, **4**, 29. Copyright @2020 Springer Nature. (E) Band gap of 2D NiO, in comparison to other WBG 2D metal chalcogenides and halide systems.[20,62] Adapted in part with permission from Haque, F.; Daeneke, T.; Kalantar-zadeh, K.; et al. Two-Dimensional Transition Metal Oxide and Chalcogenide-Based Photocatalysts. *Nano-Micro Lett.* 2018, **10**, 23. Copyright @2018 Springer Nature.

from NiO, while the peak area in red (area B) could be the contribution of Ni^{2+} from $Ni(OH)_2$ or Ni^{3+} from Ni_2O_3, of which the Ni ions have very close binding energy and thus very hard to distinguish one from the other.[38,43] Area B may also include the secondary electrons from area A, which is an inherent characteristic of XPS.[44] Therefore, the peak area ratio B/A is discussed and analyzed (Figure 4D) instead of the exact peak area to track the relative amount of NiO formed during the conversion and to investigate the chemical reactions occurring under different temperature ranges. In general, the B/A values obtained from Ni $2p_{3/2}$ and O 1s show similar trends, which increase first in the lower temperature range (below 500 °C, stage I), then dramatically decrease in the medium temperature range (500 to 800 °C, stage II), and eventually stabilize in the higher temperature range (above 800 °C, stage III). During **stage I**, the formation of both NiO and Ni_2O_3 happens, which increases B and A values simultaneously, resulting in the overall B/A value increase. When the temperature continues to increase (**stage II**), Ni_2O_3 starts to decompose and generates NiO and O_2 due to its poor thermal stability at high temperatures (~600 °C),[42] leading to a lower B and higher A, and thus gives an overall decreasing B/A value. After the Ni_2O_3 decomposition is complete (**stage III**), the B/A value stabilizes, and the generated O_2 leaves the material and creates oxygen vacancies (V_{oxy}) in the crystals.

Electronic Structure Characterization of 2D NiO. The conversion process from the initial 2D α-$Ni(OH)_2$ to NiO is then tracked using XAS at the O K edge (Figure 5A, orange) and the Ni L edge (Figure S11). Combined with nonresonant XES at the O K edge (Figure 5A, blue), the band gap of each sample annealed at different temperatures is estimated.[45,46] As can be seen from Figure 5A, the O K edge changes in structure, with the peak shifting from 533.5 eV for α-$Ni(OH)_2$ (purple arrow) to 532.5 eV in NiO-300 (green arrow). Higher temperature annealing results in sharper features appearing at higher energies, which is attributed to the healing of defects as the NiO sample approaches its bulk counterpart.[47] The Ni L edge shown in Figure S11 does not show evidence of strong sensitivity to whether the material is in the $Ni(OH)_2$ or NiO phase, which we attribute to the lack of change of symmetry and charge at the Ni^{2+} site.[48]

The band edges are determined using the second derivative method (Figure 5A, dashed lines),[49] where the onset (short orange lines for absorption and short blue lines for emission) of the conduction (valence) band is determined by the first peak in the rising spectral edge above the noise level, corresponding to the change in the concavity of the onset absorption (emission) spectrum.[50−52] To smooth the spectra and make the estimation of the second derivative feasible, we employ a Savitzky−Golay filter using a window size of 15 data points and polynomial orders of 3 and 4 for XES and XAS data, respectively.[53] Figure 5B shows the absorption (orange dots) and emission (blue dots) band edge positions derived from Figure 5A, and the band gap is estimated by taking the difference between absorption and emission onsets for each sample, as shown in Figure 5C. Notably, to account for the core−hole final state effect in the XAS spectra, 0.3 eV is added to the core−hole screening for the O K edge.[54,55] As can be seen in Figure 5A, the band gap of the $Ni(OH)_2$ film is determined to be around 2.2 eV, which is significantly lower than the bulk value. Such exceptional deviation from the quantum size effect of nanoscale systems has been predicted from DFT calculations[56] and also observed in several other systems, such as hematite and zinc nanoparticles.[57,58]

The reason behind the deviation could be the low-lying unoccupied surface states in the conduction band arising from the O−H surface bonds. A similar effect has been reported in 6 nm FeOOH nanoparticles, where the band gap is reduced from the bulk counterpart, where the reduction in the gap is attributed to structural disorder and under coordinated oxygen sites at the particle surface.[59] In both FeOOH nanoparticles and 2D $Ni(OH)_2$ cases, surface states play a significant role in determining the band gap. A previous dual computational and experimental study of NiO (111) and (100) surfaces has demonstrated that hydroxyl desorption begins at 126 °C.[60] If the lower band gap in $Ni(OH)_2$ is due to O−H, then the removal of these states should increase the gap; this appears consistent with our XAS and XES data, where the determined band gap increases to 2.9 eV in the 100 °C annealed sample (Figure 5C).

As the sample is annealed above 100 °C, the bulk of the sample starts to convert to NiO by the removal of H_2O molecules from the bulk, resulting in the formation of vacancies, while under atmospheric conditions, the sample is reoxidized by ambient O_2. The 2D NiO sample with the highest band gap is from annealing at 1000 °C and the determined gap is 2.75 ± 0.24 eV, while the values for the other 2D NiO samples hover between 2.0 and 2.72 eV. Other studies have also found band gaps in nanostructured NiO to be less than the bulk value.[61] In comparing the band gap of 2D NiO with other reported WBG 2D oxides (Figure 5D),[62,63] we determine that the gap sits firmly in the middle range of MOs and at the higher end of metal chalcogenides and halide systems (Figure 5E).[20,62]

CONCLUSIONS

In conclusion, we achieve the largest ever reported 2D NiO (>10 μm) down to a few nanometers through a thermal conversion of 2D $Ni(OH)_2$, with a comprehensive understanding of the process. This conversion from a vdW to a non-vdW structure not only sets a precedent for producing more 2D non-vdW materials but also unveils insights into morphology, structural variations, and chemical reactions during the process, offering valuable guidance for material design, integration, and manufacturing. Moreover, the band gap of the thermally converted 2D Ni_xO_y (E_g > 2.7 eV) is observed to be higher than that of the starting material 2D α-$Ni(OH)_2$, affirming the position of 2D NiO within the WBG 2D semiconductor family. The electronic band structure of Ni_xO_y (E_g > 2.7 eV), examined by soft X-ray spectroscopies, XAS and XES, contributes valuable knowledge to the understanding of this material type. Considering the simplicity, great reproducibility, and industrial fabrication process compatibility of the thermal conversion method, our work demonstrates a promising pathway for producing non-vdW 2D materials from layered precursors, thereby expanding the 2D material family. The pivotal results on 2D NiO suggest its potential as a WBG semiconductor for high-voltage operation in future micro-/nanoelectronics.

METHODS

Thermal Conversion. The thermal conversion takes place in a mostly enclosed oven from Thermo Scientific (Lindberg/Blue M Moldatherm Box Furnace, 5.3L), in which the air can only exchange with the reservoir via a 10 cm diameter hole.

Chemicals and Materials. 2D $Ni(OH)_2$ flakes used for thermal conversion are from our previous work.[30]

Characterization Techniques. Optical images are captured using an optical microscope (Nikon DS-Ri2). AFM topography is acquired on a Bruker Dimension 3000 in tapping mode. TGA is measured on an SDT Q600 from TA Instruments. XPS spectra are collected from Thermo Scientific Nexsa. TEM measurements are performed on an FEI Tecnai Osiris transmission electron microscope, operating at a 200 keV accelerating voltage. SAED is also measured on an FEI Tecnai Osiris transmission electron microscope. For the deep UV Raman system, a 266 nm (4.66 eV) laser excitation is used, and the spectrum is collected from a custom-built micro-Raman setup. The laser beam is directed onto the sample through a 40× ultraviolet objective lens (Thorlabs, LMU-40X-UVB), with a laser spot size of 1 μm. The Raman signal is collected using the same objective lens, focused into a 230 μm core fiber, and transmitted to a spectrometer (Jobin-Yvan, FNR640) equipped with a TE-cooled CCD (Andor, Newton).[64] Soft XAS and XES are carried out at the Advanced Light Source (ALS) at Lawrence Berkeley National Laboratory on beamline 8.0.1. using the iRIXS endstation. XAS is performed at the O K edge and Ni L edge, and XES measurements (excitation energy = 600 eV) are measured at the O K edge.[65]

ASSOCIATED CONTENT

Supporting Information

The Supporting Information is available free of charge at https://pubs.acs.org/doi/10.1021/acsomega.4c03253.

AFM characterization for thickness measurements on 5 different flakes (S1−S5); TGA from starting to 500 °C (S6); low-magnification TEM images of 2D $Ni(OH)_2$ (S7); separate XPS Ni 2p spectra (S8); XPS O 1s spectra (S9); separate XPS O 1s spectra (S10); and Ni L edge XAS (S11) (PDF)

AUTHOR INFORMATION

Corresponding Authors

Kevin E. Smith − *Division of Materials Science and Engineering, Boston University, Boston, Massachusetts 02215, United States; Department of Physics, Boston University, Boston, Massachusetts 02215, United States;* orcid.org/0000-0002-9076-7429; Email: ksmith@bu.edu

Xi Ling − *Division of Materials Science and Engineering, Boston University, Boston, Massachusetts 02215, United*

States; Department of Chemistry, Boston University, Boston, Massachusetts 02215, United States; The Photonics Center, Boston University, Boston, Massachusetts 02215, United States; orcid.org/0000-0003-3462-9088; Email: xiling@bu.edu

Authors

Lu Ping – *Division of Materials Science and Engineering, Boston University, Boston, Massachusetts 02215, United States*

Nicholas Russo – *Department of Physics, Boston University, Boston, Massachusetts 02215, United States;* orcid.org/0000-0001-7561-9041

Zifan Wang – *Department of Chemistry, Boston University, Boston, Massachusetts 02215, United States*

Ching-Hsiang Yao – *Department of Chemistry, Boston University, Boston, Massachusetts 02215, United States*

Complete contact information is available at:
https://pubs.acs.org/10.1021/acsomega.4c03253

Author Contributions

[⊥]L.P. and N.R. are contributed equally to this work.

Author Contributions

L.P., N.R., and X.L. conceived and designed the experiments. L.P. performed all the synthesis. L.P., N.R., Z.W., and C.Y. characterized the samples. L.P., N.R., K.S., and X.L. analyzed the data and wrote the manuscript. All authors discussed the results and commented on the manuscript.

Notes

The authors declare no competing financial interest.

■ ACKNOWLEDGMENTS

The donors of the American Chemical Society Petroleum Research Fund under Grant No. PRF# 61965-ND10 are acknowledged for support of this research. L.P., N.R., K.S., and X.L. acknowledge the support of the National Science Foundation (NSF) under Grant No. 2216008. Work done by X.L. and Z.F.W. is also supported by the U.S. Department of Energy (DOE), Office of Science, Basic Energy Science (BES) under Award Number DE-SC0021064, and the NSF under Grant No. 1945364. We thank Professor Yu-Ming Chang from National Taiwan University for using his deep ultraviolet Raman system for a portion of this work. This research uses resources from the Center for Nanoscale Systems, Harvard University, and the Center of Condensed Matter Sciences, National Taiwan University. This research also uses resources from the Advanced Light Source, which is a DOE Office of Science User Facility under contract no. DE-AC02-05CH11231. We acknowledge Dr. Haoxuan Yan for helping with the TGA measurement.

■ REFERENCES

(1) Varley, J. B.; Shen, B.; Higashiwaki, M. Wide Bandgap Semiconductor Materials and Devices. *J. Appl. Phys.* **2022**, *131* (23), 1633–1636.

(2) Cao, Y.; Pomeroy, J. W.; Uren, M. J.; Yang, F.; Kuball, M. Electric Field Mapping of Wide-Bandgap Semiconductor Devices at a Submicrometre Resolution. *Nat. Electron.* **2021**, *4* (7), 478–485.

(3) Kumar, R.; Aggarwal, V.; Yadav, A.; Gautam, S.; Singh, S.; Ganesan, R.; Singh Awana, V. P.; Gupta, G.; Muthusamy, S. K.; Kushvaha, S. S. Topological Bi2Se3/n-GaN Hybrid Structure for Enhanced and Self-Powered UV Photodetectors. *ACS Appl. Electron. Mater.* **2023**, *5* (7), 3981–3992.

(4) Zhou, X.; Lu, Z.; Zhang, L.; Ke, Q. Wide-Bandgap All-Inorganic Lead-Free Perovskites for Ultraviolet Photodetectors. *Nano Energy* **2023**, *117* (7), No. 108908.

(5) Ballestín-Fuertes, J.; Muñoz-Cruzado-alba, J.; Sanz-Osorio, J. F.; Laporta-Puyal, E. Role of Wide Bandgap Materials in Power Electronics for Smart Grids Applications. *Electronics* **2021**, *10* (6), 677.

(6) Mak, K. F.; Lee, C.; Hone, J.; Shan, J.; Heinz, T. F. Atomically Thin MoS2: A New Direct-Gap Semiconductor. *Phys. Rev. Lett.* **2010**, *105* (13), 2–5.

(7) Li, L.; Yu, Y.; Ye, G. J.; Ge, Q.; Ou, X.; Wu, H.; Feng, D.; Chen, X. H.; Zhang, Y. Black Phosphorus Field-Effect Transistors. *Nat. Nanotechnol.* **2014**, *9* (5), 372–377.

(8) Wang, Q. H.; Kalantar-Zadeh, K.; Kis, A.; Coleman, J. N.; Strano, M. S. Electronics and Optoelectronics of Two-Dimensional Transition Metal Dichalcogenides. *Nat. Nanotechnol.* **2012**, *7* (11), 699–712.

(9) Tan, C.; Cao, X.; Wu, X. J.; He, Q.; Yang, J.; Zhang, X.; Chen, J.; Zhao, W.; Han, S.; Nam, G. H.; Sindoro, M.; Zhang, H. Recent Advances in Ultrathin Two-Dimensional Nanomaterials. *Chem. Rev.* **2017**, *117* (9), 6225–6331.

(10) Nicolosi, V.; Chhowalla, M.; Kanatzidis, M. G.; Strano, M. S.; Coleman, J. N. Liquid Exfoliation of Layered Materials. *Science (80-.).* **2013**, *340* (6139), 72–75.

(11) Gong, C.; Hu, K.; Wang, X.; Wangyang, P.; Yan, C.; Chu, J.; Liao, M.; Dai, L.; Zhai, T.; Wang, C.; Li, L.; Xiong, J. 2D Nanomaterial Arrays for Electronics and Optoelectronics. *Adv. Funct. Mater.* **2018**, *28* (16), 1–23.

(12) Zhou, J.; Shen, L.; Costa, M. D.; Persson, K. A.; Ong, S. P.; Huck, P.; Lu, Y.; Ma, X.; Chen, Y.; Tang, H.; Feng, Y. P. 2DMatPedia, an Open Computational Database of Two-Dimensional Materials from Top-down and Bottom-up Approaches. *Sci. Data* **2019**, *6* (1), 1–10.

(13) Wang, G.; Chernikov, A.; Glazov, M. M.; Heinz, T. F.; Marie, X.; Amand, T.; Urbaszek, B. Colloquium: Excitons in Atomically Thin Transition Metal Dichalcogenides. *Rev. Mod. Phys.* **2018**, *90* (2), 21001.

(14) Radisavljevic, B.; Radenovic, A.; Brivio, J.; Giacometti, V.; Kis, A. Single-Layer MoS2 Transistors. *Nat. Nanotechnol.* **2011**, *6* (3), 147–150.

(15) Huang, Y.; Sutter, E.; Sadowski, J. T.; Cotlet, M.; Monti, O. L. A.; Racke, D. A.; Neupane, M. R.; Wickramaratne, D.; Lake, R. K.; Parkinson, B. A.; Sutter, P. Tin Disulfide-an Emerging Layered Metal Dichalcogenide Semiconductor: Materials Properties and Device Characteristics. *ACS Nano* **2014**, *8* (10), 10743–10755.

(16) Li, L.; Chen, Z.; Hu, Y.; Wang, X.; Zhang, T.; Chen, W.; Wang, Q. Single-Layer Single-Crystalline SnSe Nanosheets. *J. Am. Chem. Soc.* **2013**, *135* (4), 1213–1216.

(17) Zhu, Q.; Li, J.; Simon, P.; Xu, B. Two-Dimensional MXenes for Electrochemical Capacitor Applications: Progress, Challenges and Perspectives. *Energy Storage Mater.* **2021**, *35*, 630–660.

(18) Anasori, B.; Lukatskaya, M. R.; Gogotsi, Y. 2D Metal Carbides and Nitrides (MXenes) for Energy Storage. *Nat. Rev. Mater.* **2017**, *2* (2). DOI: .

(19) Woods-Robinson, R.; Han, Y.; Zhang, H.; Ablekim, T.; Khan, I.; Persson, K. A.; Zakutayev, A. Wide Band Gap Chalcogenide Semiconductors. *Chem. Rev.* **2020**, *120* (9), 4007–4055.

(20) Lu, Y.; Warner, J. H. Synthesis and Applications of Wide Bandgap 2D Layered Semiconductors Reaching the Green and Blue Wavelengths. *ACS Appl. Electron. Mater.* **2020**, *2* (7), 1777–1814.

(21) Zhou, K.; Shang, G.; Hsu, H. H.; Han, S. T.; Roy, V. A. L.; Zhou, Y. Emerging 2D Metal Oxides: From Synthesis to Device Integration. *Adv. Mater.* **2023**, *35* (21), 1–42.

(22) Zhang, B. Y.; Xu, K.; Yao, Q.; Jannat, A.; Ren, G.; Field, M. R.; Wen, X.; Zhou, C.; Zavabeti, A.; Ou, J. Z. Hexagonal Metal Oxide Monolayers Derived from the Metal–Gas Interface. *Nat. Mater.* **2021**, *20* (8), 1073–1078.

(23) Rui, X.; Lu, Z.; Yu, H.; Yang, D.; Hng, H. H.; Lim, T. M.; Yan, Q. Ultrathin V2O5 Nanosheet Cathodes: Realizing Ultrafast Reversible Lithium Storage. *Nanoscale* **2013**, *5* (2), 556−560.

(24) Zhao, S.; Zhang, J.; Fu, L. Liquid Metals: A Novel Possibility of Fabricating 2D Metal Oxides. *Adv. Mater.* **2021**, *33* (9), 1−14.

(25) Zavabeti, A.; Ou, J. Z.; Carey, B. J.; Syed, N.; Orrell-Trigg, R.; Mayes, E. L. H.; Xu, C.; Kavehei, O.; O'Mullane, A. P.; Kaner, R. B.; Kalantar-Zadeh, K.; Daeneke, T. A Liquid Metal Reaction Environment for the Room-Temperature Synthesis of Atomically Thin Metal Oxides. *Science (80-.).* **2017**, *358* (6361), 332−335.

(26) Hai, Z.; Akbari, M. K.; Xue, C.; Xu, H.; Hyde, L.; Zhuiykov, S. Wafer-Scaled Monolayer WO 3 Windows Ultra-Sensitive, Extremely-Fast and Stable UV-A Photodetection. *Appl. Surf. Sci.* **2017**, *405*, 169−177.

(27) Yuan, J.; Balk, A.; Guo, H.; Fang, Q.; Patel, S.; Zhao, X.; Terlier, T.; Natelson, D.; Crooker, S.; Lou, J. Room-Temperature Magnetic Order in Air-Stable Ultrathin Iron Oxide. *Nano Lett.* **2019**, *19* (6), 3777−3781.

(28) Yin, C.; Gong, C.; Chu, J.; Wang, X.; Yan, C.; Qian, S.; Wang, Y.; Rao, G.; Wang, H.; Liu, Y.; Wang, X.; Wang, J.; Hu, W.; Li, C.; Xiong, J. Ultrabroadband Photodetectors up to 10.6 Mm Based on 2D Fe3O4 Nanosheets. *Adv. Mater.* **2020**, *32* (25), 4−11.

(29) Liu, A.; Meng, Y.; Zhu, H.; Noh, Y. Y.; Liu, G.; Shan, F. Electrospun P-Type Nickel Oxide Semiconducting Nanowires for Low-Voltage Field-Effect Transistors. *ACS Appl. Mater. Interfaces* **2018**, *10* (31), 25841−25849.

(30) Ping, L.; Minarik, G. E.; Gao, H.; Cao, J.; Li, T.; Kitadai, H.; Ling, X. Synthesis of 2D Layered Transition Metal (Ni, Co) Hydroxides via Edge-on Condensation. *Sci. Rep.* **2024**, *14* (1), 3817.

(31) Qiu, J.; Nguyen, T. H.; Lee, Y. J.; Kim, S.; Kim, S.; Kim, S. J.; Song, M. T.; Huang, W. J.; Chen, X. B.; Yang, I. S. Strong Oxygen-Content Dependence of the Magnetic Excitations in Antiferromagnetic NiO Nanoparticles: A Raman Probe. *Spectrochim. Acta, Part A* **2023**, *297*, No. 122700.

(32) Mironova-Ulmane, N.; Kuzmin, A.; Sildos, I.; Puust, L.; Grabis, J. Magnon and Phonon Excitations in Nanosized NiO. *Latv. J. Phys. Technol. Sci.* **2019**, *56* (2), 61−72.

(33) Tian, J.; Xue, Y.; Yu, X.; Pei, Y.; Zhang, H.; Wang, J. 2D Nanoporous Ni(OH)2 Film as an Electrode Material for High-Performance Energy Storage Devices. *RSC Adv.* **2019**, *9* (31), 17706−17716.

(34) Kim, S. J.; Jo, S. G.; Lee, E. B.; Lee, J. W. Morphology-Controlled Nickel Oxide and Iron-Nickel Oxide for Electrochemical Oxygen Evolution Reaction. *ACS Appl. Energy Mater.* **2023**, *6*, 8360.

(35) Cai, X.; Shen, X.; Ma, L.; Ji, Z.; Xu, C.; Yuan, A. Solvothermal Synthesis of NiCo-Layered Double Hydroxide Nanosheets Decorated on RGO Sheets for High Performance Supercapacitor. *Chem. Eng. J.* **2015**, *268*, 251−259.

(36) He, F.; Hu, Z.; Liu, K.; Zhang, S.; Liu, H.; Sang, S. In Situ Fabrication of Nickel Aluminum-Layered Double Hydroxide Nanosheets/Hollow Carbon Nanofibers Composite as a Novel Electrode Material for Supercapacitors. *J. Power Sources* **2014**, *267*, 188−196.

(37) Rani, J. R.; Thangavel, R.; Kim, M.; Lee, Y. S.; Jang, J. H. Ultra-High Energy Density Hybrid Supercapacitors Using Mno2/Reduced Graphene Oxide Hybrid Nanoscrolls. *Nanomaterials* **2020**, *10* (10), 2049.

(38) Blume, A. R.; Calvet, W.; Ghafari, A.; Mayer, T.; Knop-Gericke, A.; Schlögl, R. Structural and Chemical Properties of NiOx Thin Films: The Role of Oxygen Vacancies in NiOOH Formation in a H2O Atmosphere. *Phys. Chem. Chem. Phys.* **2023**, *25*, 25552−25565.

(39) Liu, A.; Liu, G.; Zhu, H.; Shin, B.; Fortunato, E.; Martins, R.; Shan, F. Hole Mobility Modulation of Solution-Processed Nickel Oxide Thin-Film Transistor Based on High-k Dielectric. *Appl. Phys. Lett.* **2016**, *108* (23), 1−6.

(40) Chia-Ching, W.; Cheng-Fu, Y. Investigation of the Properties of Nanostructured Li-Doped NiO Films Using the Modified Spray Pyrolysis Method. *Nanoscale Res. Lett.* **2013**, *8* (1), 1−5.

(41) Zhang, H.; Zhao, C.; Yao, J.; Choy, W. C. H. Dopant-Free NiOx Nanocrystals: A Low-Cost and Stable Hole Transport Material for Commercializing Perovskite Optoelectronics. *Angew. Chemie - Int. Ed.* **2023**, *62* (24). DOI: .

(42) Zhou, L.; Rai, A.; Piekiel, N.; Ma, X.; Zachariah, M. R. Ion-Mobility Spectrometry of Nickel Nanoparticle Oxidation Kinetics: Application to Energetic Materials. *J. Phys. Chem. C* **2008**, *112* (42), 16209−16218.

(43) Koshtyal, Y.; Nazarov, D.; Ezhov, I.; Mitrofanov, I.; Kim, A.; Rymyantsev, A.; Lyutakov, O.; Popovich, A.; Maximov, M. Atomic Layer Deposition of Nio to Produce Active Material for Thin-Film Lithium-Ion Batteries. *Coatings* **2019**, *9* (5). DOI: 301.

(44) Vilan, A.; Bendikov, T. A.; Cohen, H. Secondary Electron Emission Control in X-Ray Photoelectron Spectroscopy. *J. Electron Spectrosc. Relat. Phenom.* **2008**, *162* (2), 99−105.

(45) Preston, A. R. H.; Ruck, B. J.; Piper, L. F. J.; DeMasi, A.; Smith, K. E.; Schleife, A.; Fuchs, F.; Bechstedt, F.; Chai, J.; Durbin, S. M. Band Structure of ZnO from Resonant X-Ray Emission Spectroscopy. *Phys. Rev. B* **2008**, *78* (15), No. 155114.

(46) Piper, L. F. J.; Colakerol, L.; Learmonth, T.; Glans, P.-A.; Smith, K. E.; Fuchs, F.; Furthmüller, J.; Bechstedt, F.; Chen, T.-C.; Moustakas, T. D.; Guo, J.-H. Electronic Structure of {InN} Studied Using Soft X-Ray Emission, Soft x-Ray Absorption, and Quasiparticle Band Structure Calculations. *Phys. Rev. B* **2007**, *76* (24), No. 245204.

(47) Soriano, L.; Abbate, M.; Fernández, A.; González-Elipe, A. R.; Sirotti, F.; Rossi, G.; Sanz, J. M. Thermal Annealing of Defects in Highly Defective NiO Nanoparticles Studied by X-Ray and Electron Spectroscopies. *Chem. Phys. Lett.* **1997**, *266* (1−2), 184−188.

(48) Rooksby, H. P. A Note on the Structure of Nickel Oxide at Subnormal and Elevated Temperatures. *Acta Crystallogr.* **1948**, *1* (4), 226−226.

(49) Kurmaev, E. Z.; Wilks, R. G.; Moewes, A.; Finkelstein, L. D.; Shamin, S. N.; Kuneš, J. Oxygen X-Ray Emission and Absorption Spectra as a Probe of the Electronic Structure of Strongly Correlated Oxides. *Phys. Rev. B* **2008**, *77* (16), No. 165127.

(50) McLeod, J. A.; Green, R. J.; Kurmaev, E. Z.; Kumada, N.; Belik, A. A.; Moewes, A. Band-Gap Engineering in TiO2-Based Ternary Oxides. *Phys. Rev. B* **2012**, *85* (19), No. 195201.

(51) Al Fattah, M. F.; Amin, M. R.; Mallmann, M.; Kasap, S.; Schnick, W.; Moewes, A. Electronic Structure Investigation of Wide Band Gap Semiconductors—Mg2PN and Zn2PN: Experiment and Theory. *J. Phys.: Condens. Matter* **2020**, *32* (40), No. 405504.

(52) Amin, M. R.; De Boer, T.; Becker, P.; Hertrampf, J.; Niewa, R.; Moewes, A. Bandgap and Electronic Structure Determination of Oxygen-Containing Ammonothermal InN: Experiment and Theory. *J. Phys. Chem. C* **2019**, *123* (14), 8943−8950.

(53) Savitzky, A.; Golay, M. J. E. Smoothing and Differentiation of Data. *Anal. Chem.* **1964**, *36* (8), 1627−1639.

(54) Frati, F.; Hunault, M. O. J. Y.; de Groot, F. M. F. Oxygen K-Edge X-Ray Absorption Spectra. *Chem. Rev.* **2020**, *120* (9), 4056−4110.

(55) Zhang, L.; Schwertfager, N.; Cheiwchanchamnangij, T.; Lin, X.; Glans-Suzuki, P.-A.; Piper, L. F. J.; Limpijumnong, S.; Luo, Y.; Zhu, J. F.; Lambrecht, W. R. L.; Guo, J.-H. Electronic Band Structure of Graphene from Resonant Soft X-Ray Spectroscopy: {The} Role of Core-Hole Effects. *Phys. Rev. B* **2012**, *86* (24), No. 245430.

(56) Nagli, M.; Caspary Toroker, M. Communication: Nickel Hydroxide as an Exceptional Deviation from the Quantum Size Effect. *J. Chem. Phys.* **2018**, *149* (14). DOI: .

(57) Gilbert, B.; Frandsen, C.; Maxey, E. R.; Sherman, D. M. Band-Gap Measurements of Bulk and Nanoscale Hematite by Soft x-Ray Spectroscopy. *Phys. Rev. B - Condens. Matter Mater. Phys.* **2009**, *79* (3), 1−7.

(58) Dong, C. L.; Persson, C.; Vayssieres, L.; Augustsson, A.; Schmitt, T.; Mattesini, M.; Ahuja, R.; Chang, C. L.; Guo, J. H. Electronic Structure of Nanostructured ZnO from X-Ray Absorption and Emission Spectroscopy and the Local Density Approximation. *Phys. Rev. B - Condens. Matter Mater. Phys.* **2004**, *70* (19), 1−5.

(59) Gilbert, B.; Kim, C. S.; Dong, C. L.; Guo, J.; Nico, P. S.; Shuh, D. K. Oxygen K-Edge Emission and Absorption Spectroscopy of Iron Oxyhydroxide Nanoparticles. *AIP Conf. Proc.* **2007**, *882*, 721−725.

(60) Zhao, W.; Bajdich, M.; Carey, S.; Vojvodic, A.; Nørskov, J. K.; Campbell, C. T. Water Dissociative Adsorption on NiO(111): Energetics and Structure of the Hydroxylated Surface. *ACS Catal.* **2016**, *6* (11), 7377−7384.

(61) Alammar, T.; Shekhah, O.; Wohlgemuth, J.; Mudring, A. V. Ultrasound-Assisted Synthesis of Mesoporous β-Ni(OH)2 and NiO Nano-Sheets Using Ionic Liquids. *J. Mater. Chem.* **2012**, *22* (35), 18252−18260.

(62) Chaves, A.; Azadani, J. G.; Alsalman, H.; da Costa, D. R.; Frisenda, R.; Chaves, A. J.; Song, S. H.; Kim, Y. D.; He, D.; Zhou, J.; Castellanos-Gomez, A.; Peeters, F. M.; Liu, Z.; Hinkle, C. L.; Oh, S. H.; Ye, P. D.; Koester, S. J.; Lee, Y. H.; Avouris, P.; Wang, X.; Low, T. Bandgap Engineering of Two-Dimensional Semiconductor Materials. *npj 2D Mater. Appl.* **2020**, *4* (1). DOI: .

(63) Haque, F.; Daeneke, T.; Kalantar-zadeh, K.; Ou, J. Z. Two-Dimensional Transition Metal Oxide and Chalcogenide-Based Photocatalysts. *Nano-Micro Lett.* **2018**, *10* (2), 1−27.

(64) Gulo, D. P.; Hung, N. T.; Chen, W. L.; Wang, S.; Liu, M.; Kauppinen, E. I.; Maruyama, S.; Chang, Y. M.; Saito, R.; Liu, H. L. Interacting Phonons between Layers in Raman Spectra of Carbon Nanotubes inside Boron Nitride Nanotubes. *J. Phys. Chem. Lett.* **2023**, *14* (45), 10263−10270.

(65) Qiao, R.; Li, Q.; Zhuo, Z.; Sallis, S.; Fuchs, O.; Blum, M.; Weinhardt, L.; Heske, C.; Pepper, J.; Jones, M.; Brown, A.; Spucces, A.; Chow, K.; Smith, B.; Glans, P.-A.; Chen, Y.; Yan, S.; Pan, F.; Piper, L. F. J.; Denlinger, J.; Guo, J.; Hussain, Z.; Chuang, Y.-D.; Yang, W. High-Efficiency in Situ Resonant Inelastic x-Ray Scattering (iRIXS) Endstation at the Advanced Light Source. *Rev. Sci. Instrum.* **2017**, *88* (3), 33106.